Rechargeable Co₃O₄ porous nanoflake carbon nanotube nanocomposite lithium-ion battery anodes with enhanced energy performances†

Song Qiu,[a] Hongbo Gu,[b] Guixia Lu,[a] Jiurong Liu,*[a] Xiaoyu Li,[a] Ya Fu,[a] Xingru Yan,[c] Chenxi Hu[a] and Zhanhu Guo*[c]

Multi-walled carbon nanotubes intertwined with porous Co₃O₄ nanoflakes (Co₃O₄/MWNT) have been hydrothermally synthesized to form a three dimensional network with superior electrical and ionic conductivity and tested as an anode material for lithium-ion batteries (LIBs). The electrochemical measurements on the Co₃O₄/MWNT composites demonstrated a reversible capacity of 708 mA h g⁻¹ after 100 cycles at a current density of 100 mA g⁻¹ and discharge capacities of 773, 805, 698, and 491 mA h g⁻¹ at current densities of 100, 200, 400, and 800 mA g⁻¹, respectively. The superior cycling and rate performances were attributed to the formed network structure, in which the entanglement and flexibility of MWNTs buffered the volume change of Co₃O₄ during the charge–discharge process and improved the electrical conductivity of the electrode.

1. Introduction

Rechargeable lithium-ion batteries (LIBs) are the leading power sources for popular consumer electronics and upcoming electrical/hybrid vehicles.[1,2] However, the currently used commercial graphite anodes have a low theoretical capacity of 372 mA h g⁻¹, which limits their use in applications that demand high energy density.[3] Nanosized transition metal oxides (such as Fe₃O₄, CoO, Co₃O₄, CuO, TiO₂, NiO, MnO₂) are considered to be promising electrode materials due to their high theoretical capacities.[4–6] Among them, Co₃O₄ is a potential anode material due to its high theoretical capacity (890 mA h g⁻¹), two times larger than that of graphite as aforementioned. For example, Sun *et al.*[7] reported that hollow spherical Co₃O₄ thin films exhibited a first-discharge capacity of 1424 mA h g⁻¹, a reversible capacity of above 1000 mA h g⁻¹ for up to 50 cycles and good rate capability. Zhang *et al.*[8] synthesized three kinds of Co₃O₄ nanomaterials, *i.e.*, nanorods, nanoclusters and nanoplates. The nanorod anodes showed the best performance with a stable reversible capacity of 954 mA h g⁻¹ after 35 cycles, but the other two anodes including nanoclusters and nanoplates

demonstrated poor lithium storage properties. In addition, Co₃O₄ nanopowders with particle sizes of 20–30 nm prepared by Kang *et al.*[9] exhibited a capacity of 1237 and 835 mA h g⁻¹ for the first discharge and charge process, respectively. There was a drastic capacity fading from the 20th cycle. All these results demonstrated that the lithium storage property of Co₃O₄ anode materials could be enhanced by tuning the morphology of Co₃O₄. However, this strategy was complicated and did not improve the conductivity of the Co₃O₄ electrode, which results in poor rate capability. The carbon materials are introduced to enhance the electrical conductivity[10–15] and improve the electrochemical performance of the transition metal oxide anodes.[16–18] Among the carbon materials, carbon nanotubes (CNTs) have been recognized as good candidates to prepare the anodes for LIBs[19–23] due to their advantages including high electrical conductivity, chemical stability and large specific surface area.[24] Yoon *et al.*[25] fabricated Co₃O₄ nanoparticle/CNT blended anodes, which showed enhanced cycling performance and rate capability compared with the pure Co₃O₄ anodes. Zhuo *et al.*[26] found that Co₃O₄-functionalized CNT composite anodes demonstrated a remarkable specific capacity (>750 mA h g⁻¹ at a current density of 200 mA g⁻¹) and high rate capability (600 mA h g⁻¹ at 1 A g⁻¹).

In this work, the well dispersed porous Co₃O₄ nanoflake and MWNT blended anode material for LIBs has been prepared by a hydrothermal method and post-processing in Ar atmosphere at 400 °C for 4 h. The as-prepared Co₃O₄/MWNT composites illustrate an excellent lithium storage capability compared to pure Co₃O₄ nanoflakes or pure MWNTs. The electrochemical impedance spectra (EIS) demonstrated that the electrical conductivity and charge transfer of the as-prepared Co₃O₄/

[a]Key Laboratory for Liquid–Solid Structural Evolution and Processing of Materials, Ministry of Education and School of Materials Science and Engineering, Shandong University, Jinan, Shandong 250061, People's Republic of China. E-mail: jrliu@sdu.edu.cn

[b]Department of Chemistry, Tongji University, Shanghai, 200092, China

[c]Integrated Composites Lab (ICL), Department of Chemical & Biomolecular Engineering, University of Tennessee, Knoxville, TN 37996, USA. E-mail: zguo10@utk.edu

MWNT composite anodes are much better than that of pure Co_3O_4 nanoflake anodes.

2. Experimental

2.1 Materials

Cobalt nitrate ($Co(NO_3)_2 \cdot 6H_2O$), urea ($CO(NH_2)_2$), polyvinyl pyrrolidone (PVP, K30), concentrated nitric acid (HNO_3) and MWNTs were purchased from Sinopharm Chemical Reagent Co., Ltd. Carbon black, Li foil and Celgard 2300 were obtained from Hefei Kejing Material Technology Co., Ltd, China. Poly-vinylidene fluoride (PVDF), 1 M $LiPF_6$ (dissolved in ethylene carbonate, dimethyl carbonate, and ethylene methyl carbonate with a volume ratio of 1 : 1 : 1) were provided by Shenzhen Biyuan Technology Co., Ltd, China. All the chemicals were in analytical grade and used as-received without any further purification.

2.2 Preparation of Co_3O_4/MWNT nanocomposites and pure Co_3O_4 nanoflakes

MWNTs were pretreated in concentrated nitric acid at 140 °C for 6 h, and then centrifuged and washed with deionized water and ethanol to neutral. In a typical synthesis procedure, MWNT (0.02 g) were dispersed in 10 mL deionized water under ultra-sonic treatment for 30 min. Then, $Co(NO_3)_2 \cdot 6H_2O$ (0.15 g), urea (0.5 g) and PVP (0.1 g) were dissolved in the slurry under magnetic stirring for 1 h. At last, the slurry was transferred into a 30 mL Teflon-lined stainless steel autoclave, subsequently sealed and heated at 180 °C for 12 h in an oven. After reaction, the precursor was centrifuged and washed with deionized water and ethanol several times, and then dried under vacuum at 60 °C for 24 h. The Co_3O_4/MWNT nanocomposites were received by heat treatment of the precursor at 400 °C for 4 h under argon atmosphere at a heating rate of 5 °C min^{-1} in a tube furnace. For comparison, the pure Co_3O_4 nanoflakes were synthesized following the same procedure without adding MWNTs. The Co_3O_4/MWNT nanocomposites, pure Co_3O_4 nanoflakes and MWNTs after treating with acid were active materials for preparing the anodes.

2.3 Measurements

The X-ray powder diffraction (XRD) patterns of the as-prepared Co_3O_4/MWNT nanocomposites, pure Co_3O_4 nanoflakes and MWNTs were obtained by a Rigaku Dmax-rc X-ray diffractom-eter with Ni filtered Cu Kα radiation ($V = 40$ kV, $I = 50$ mA) at a scanning rate of 4° min^{-1}. A JSM-6700F field emission scanning electron microscope (FE-SEM) at an accelerating voltage of 20 kV and an electric current of 1.0×10^{-10} A and A JEOL JEM-2100 high-resolution transmission electron microscopy (HR-TEM) with an accelerating voltage of 200 kV were used to examine the microstructures of the samples. The X-ray photoelectron spectra (XPS) were recorded on a Kratos Analytical spectrom-eter, using Al Kα ($h\nu = 1486.6$ eV) radiation as the excitation source, under a condition of anode voltage of 12 kV and an emission current of 10 mA. The thermal gravimetric analysis (TGA) measurement was carried out in an SDT Q600 (TA

Instruments Ltd., New Castle, DE) thermal-microbalance apparatus at a heating rate of 10 °C min^{-1} in an air atmo-sphere from ambient temperature to 800 °C to determine the percentage of carbon in the final products. The N_2 adsorption/desorption isotherms of pure MWNTs and Co_3O_4/MWNTs were measured at 77 K on a Quadrasorb-SI instrument. The specific surface area was calculated with the Brunauer–Emmett–Teller (BET) model and the pore size distribution was determined by means of the Barrett–Joyner–Halenda (BJH) method.

To prepare the working electrode, the active material, carbon black, and PVDF with a weight ratio of 8 : 1 : 1 were mixed in N-methyl-2-pyrrolidinone (NMP) to form a homogenous slurry, which was coated on a copper foil substrate, followed by drying in a vacuum oven at 120 °C for 12 h. The CR2025-type cells were assembled using Li foil as counter and reference electrode, Celgard 2300 as separator, and 1 M $LiPF_6$ as electrolyte. The assembly was performed in a glove box filled with Ar atmo-sphere. The performance of the cells was evaluated galvanos-tatically in the voltage range from 0.02 to 3 V at various current densities on a LAND CT2001A battery test system. The cyclic voltammogram (CV) was obtained on a IviumStat electro-chemistry work station with a scanning rate of 0.1 mV s^{-1} and the potential vs. Li$^+$/Li ranging from 0.01 to 3 V. The EIS were tested on the same instrument with AC signal amplitude of 10 mV in the frequency range from 100 kHz to 0.01 Hz. The data were adopted to draw Nyquist plots using real part Z′ as X-axis, and imaginary part Z″ as Y-axis.

3. Results and discussion

3.1 Characterizations of as-prepared nanocomposites

Fig. 1 illustrates the XRD patterns of the as-prepared Co_3O_4, Co_3O_4/MWNTs and pure MWNTs. As shown in Fig. 1a, all of the diffraction peaks are well indexed to that of cubic spinel phase of Co_3O_4 (JCPDS card no. 42-1467), indicating the high purity of

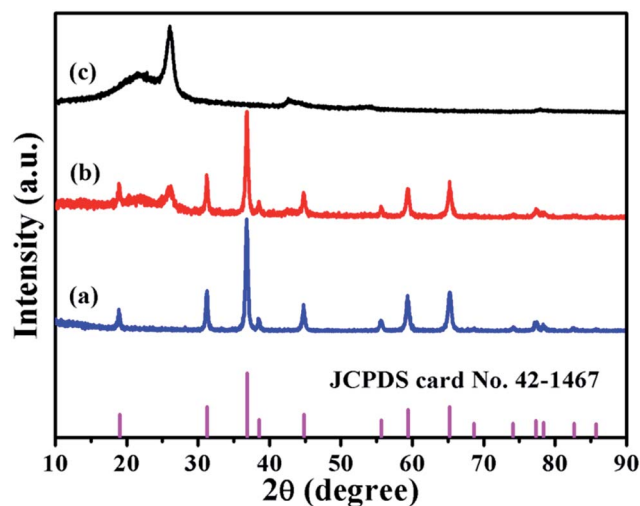Fig. 1 XRD patterns of the (a) pure Co_3O_4, (b) Co_3O_4/MWNT composite and (c) pure MWNTs.

the obtained Co_3O_4. The MWNTs (Fig. 1c) exhibit a broad diffraction peak centered at $2\theta = 22°$, indicating the existence of amorphous carbon in the CNTs.[27] The well resolved (0 0 2) diffraction line of graphite at $2\theta = 26.5°$ is also present, corresponding to (0 0 2) planes of the stacked graphene layers in the MWNTs.[28] The Co_3O_4/MWNT nanocomposites (Fig. 1b) have a mixed diffraction pattern of Co_3O_4 phase with a cubic spinel structure and pure MWNTs.

Fig. 2 displays the SEM and HR-TEM images of the as-prepared samples. The pure Co_3O_4 nanoflakes (Fig. 2a) consist of nanoparticles loosely with porous structure. Fig. 2b shows the SEM image of MWNTs after treated by nitric acid with a diameter range of 20–80 nm. As shown in Fig. 2c, the Co_3O_4 nanoflakes are observed to be dispersed in the MWNTs. The HR-TEM image (Fig. 2d) shows that the MWNTs are intertwined with the Co_3O_4 nanoflakes with pore sizes of 20–80 nm. To further confirm the porous structure of the Co_3O_4/MWNTs composites, the nitrogen adsorption/desorption measurements were performed to investigate the porosity and surface area of pure MWNTs and Co_3O_4/MWNTs (Fig. S1†). The nitrogen adsorption/desorption isotherms of the two samples can be ascribed to type IV with a distinct hysteresis loop, indicating the formation of mesoporous structures.[12] From the pore size distribution curves (inset of Fig. S1†), the pore size is observed to be in the range from 2 to 20 nm with a dominant size of *ca.* 3 nm for pure MWNTs. The pore size of Co_3O_4/MWNTs is distributed from 2 to 100 nm with dominant sizes of *ca.* 3 and 30 nm. On the base of above analysis, the pore size of the Co_3O_4 nanoflakes is in the range from 20 to 100 nm and the pores with size of *ca.* 30 nm are dominant, consistent with the HR-TEM observation. The BET specific surface area of the pure MWNTs and Co_3O_4/MWNTs is 137.5 and 45.6 m^2 g^{-1}, respectively. The porous structure of Co_3O_4/MWNTs facilitates the contact of active materials with electrolyte, inducing a fast transportation of lithium ions.

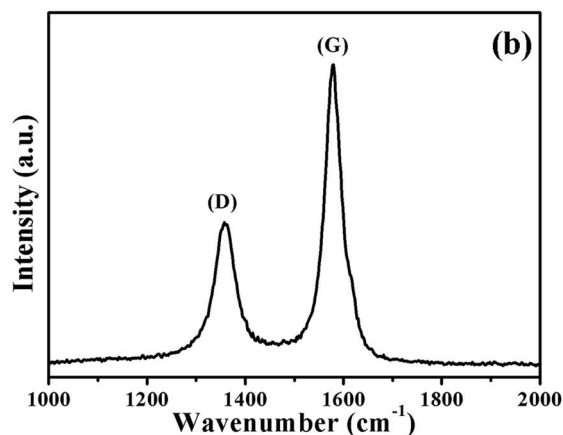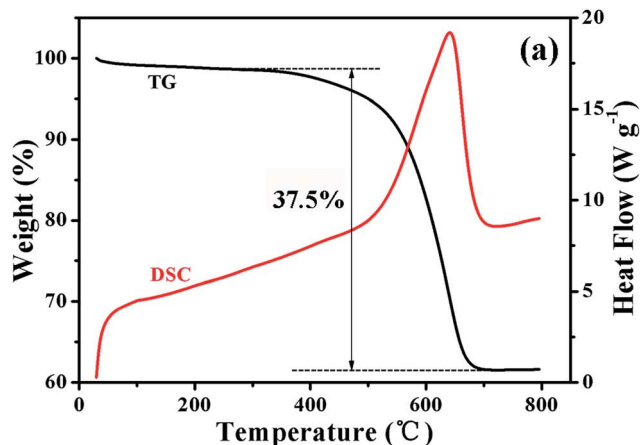To determine the amount of MWNTs in the Co_3O_4/MWNT nanocomposites, TGA analysis was carried out in air. Fig. 3a

Fig. 3 TGA and DSC curves (a) and Raman spectrum (b) of the Co_3O_4/MWNT composite.

shows the TGA curves of the Co_3O_4/MWNT nanocomposites. The rapid mass loss between 300 and 680 °C is due to the oxidation of MWNTs since Co_3O_4 is stable during this temperature range. The carbon percentage is *ca.* 37.5 wt%. The Raman spectrum of the Co_3O_4/MWNT nanocomposites is listed in Fig. 3b. The sharp peaks in the spectrum located at 1360 and 1580 cm^{-1} are assigned to the D and G bands of MWNTs, respectively. The D band originates from the defects/disordered carbons, and the G band is due to the Raman-active in-plane stretching tangential mode of the graphite sheets.[29,30] The relative intensity ratio, I_D/I_G, depends on the structural characteristics of the carbon material. The I_D/I_G value is approximately 0.4 in the prepared Co_3O_4/MWNT nanocomposites, indicating a low degree of defects in MWNTs.[31]

The XPS experiment was carried out to determine the chemical composition and valence state of Co_3O_4/MWNT nanocomposites. The survey scan in Fig. 4a shows that the surface of the nanocomposites is composed of O, Co and C elements. Fig. 4b shows the XPS spectra of Co 2p. Normally, Co_3O_4 contains two distinct types of cobalt ion: Co^{2+} in tetrahedral sites and Co^{3+} in octahedral sites with the ratio of 1 : 2.[32] It is difficult to determine the valence state of the Co by means of the binding energy alone. So the information about satellites and the spin–orbit splitting of the 2p level (ΔE) have been
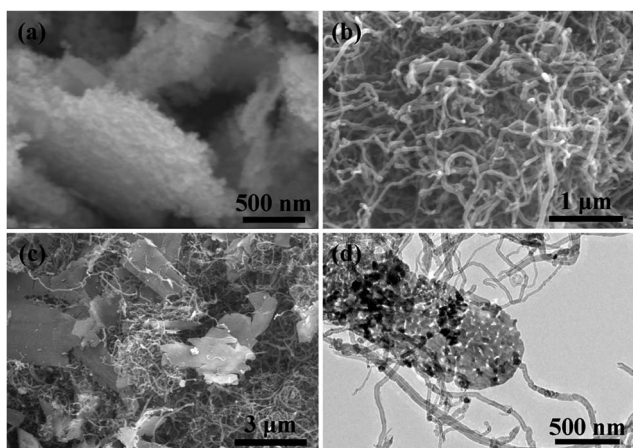

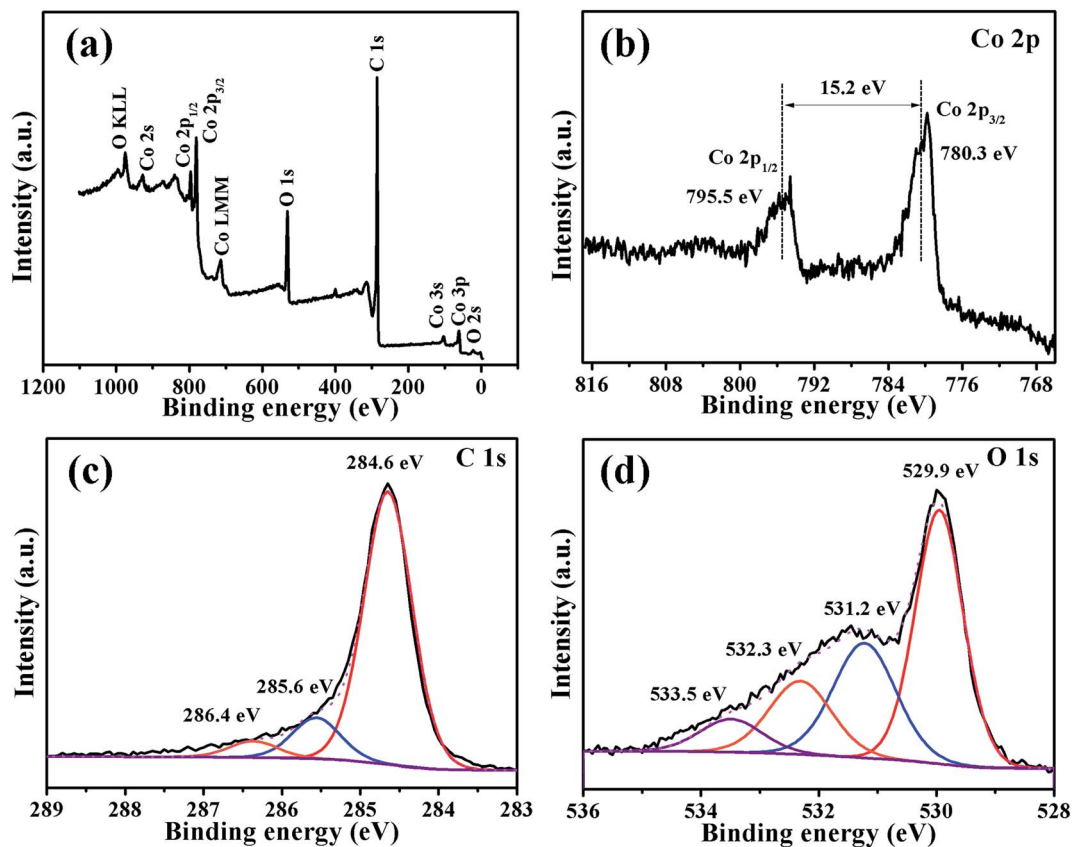Fig. 2 FE-SEM images of (a) pure Co_3O_4, (b) pure MWNT and (c) Co_3O_4/MWNT composite and HR-TEM image of (d) Co_3O_4/MWNT composite.

Fig. 4 XPS spectra of Co_3O_4/MWNT composite: (a) survey scan, (b) Co 2p, (c) C 1s and (d) O 1s.

considered. The XPS spectrum of the Co element contains two obvious peaks at 780.3 and 795.5 eV corresponding to Co $2p_{3/2}$ and Co $2p_{1/2}$, respectively. A shoulder at the high-energy side is characteristic of the Co^{2+} oxidation state, which can be traced back to a shake-up process whereas the diamagnetic low-spin Co^{3+} does not show any shake-up structures.[33,34] There is no prominent satellite structure in the XPS spectrum of the Co 2p region. The ΔE value was calculated to be 15.2 eV. Li *et al.*[34] reported that the Co_3O_4/SiO_2 catalyst containing excess Co^{2+} on its surface has the ΔE value of 15.7 eV whereas the ΔE value for the Co_3O_4/SiO_2 catalyst with stoichiometric Co_3O_4 is 15.0 eV. For our Co_3O_4/MWNT nanocomposites, the Co_3O_4 nanoflakes exhibit very weak satellite peaks and the ΔE value is 15.2 eV. These Co 2p XPS features are obviously characteristics of stoichiometric Co_3O_4.[33–36] In the C 1s spectrum (Fig. 4c), the deconvoluted peaks can be assigned to three types of carbon bonds: graphitic carbon (284.6 eV), carbon in alcohol, ether or phenol groups (C–O, 285.6 eV), and carbonyl or quinone groups (C=O, 286.4 eV), respectively.[30,37–39] The O 1s spectrum is broad and deconvoluted into four peaks centered at 529.9, 531.2, 532.3, and 533.5 eV (Fig. 4d), which are attributed to Co–O, C–O, C=O and H–O bonds, respectively.[40] The H–O bond originates from water absorbed on the surface of samples after exposure to air.

3.2 Electrochemical performance

The galvanostatic discharge–charge curves for pure Co_3O_4, pure MWNTs and Co_3O_4/MWNT nanocomposites in the potential range from 0.02 to 3.0 V *vs.* Li$^+$/Li reference electrode at the current density of 100 mA g^{-1} were tested to compare their lithium storage ability (Fig. 5a–c). The pure Co_3O_4 nanoflake electrode exhibits a specific capacity of 1197 mA h g^{-1} in the first discharge process (Fig. 5a). There are two obvious voltage plateaus at about 1.2 and 1.1 V. The initial plateau indicates the formation of rock salt CoO and amorphous Li_2O.[41] The latter relates to the transition of the intermediate into metallic cobalt.[42] With decreasing the voltage to 0.02 V, the initial discharge specific capacity (1197 mA h g^{-1}) is higher than the theoretical capacity of pure Co_3O_4, which can be attributed to the decomposition of the electrolyte and the formation of solid electrolyte interphase (SEI) films surrounding the Li_2O and cobalt nanoparticles.[43,44] The following charge curve shows no voltage plateau but a slope to 2.0 V, suggesting the oxidation of Co^0 to Co^{2+} and Co^{3+}. The first specific charge capacity is 403 mA h g^{-1}, and the initial coulombic efficiency (the ratio of charge capacity to discharge capacity) is only 34%. The irreversible capacity is attributed to the isolation and cracking of Co_3O_4 nanoflakes during the lithiation (discharge) and delithiation (charge) processes,[45,46] the irreversible formation of SEI layer in discharge,[43] the incomplete decomposition of Li_2O[47] and incomplete back formation of Co_3O_4 (ref. 48–50) during the first charge. After the initial two cycles, the Co_3O_4 electrode delivers a stable reversible capacity. The discharge specific capacity of pure MWNT cell is 532 mA h g^{-1} (Fig. 5b), much higher than the theoretical capacity of graphite (372 mA h

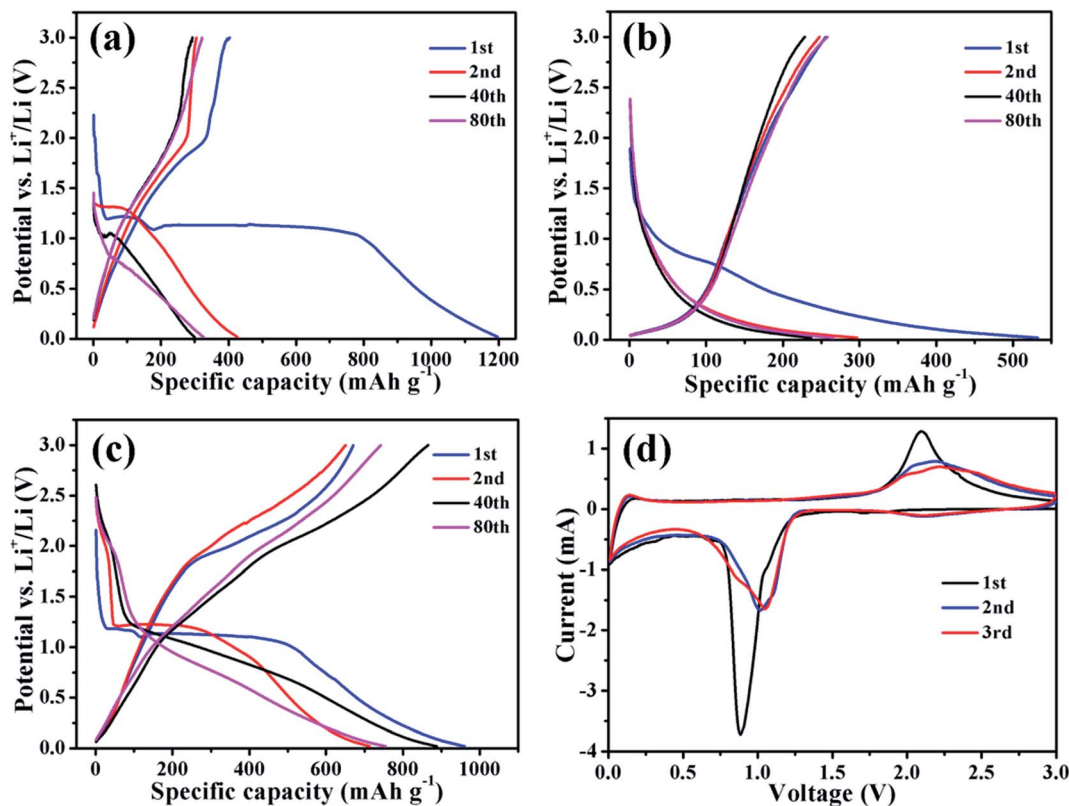Fig. 5   Galvanostatic discharge−charge curves of the 1st, 2nd, 40th, and 80th cycles for Co_3O_4 (a), MWNT (b), Co_3O_4/MWNT (c), and the CV curves of Co_3O_4/MWNT (d).

g^{-1}).[51,52] The short voltage plateau at approximately 0.8 V may be related to the formation of SEI layer on the carbon surface.[53] The first specific charge capacity is 256 mA h g^{-1}. The coulombic efficiency is 48% in the first cycle. The irreversible capacity could be related to the formation of the SEI layer and the insertion of lithium-ions into the cavities in CNTs.[53] From the second cycle, the curves are well coincided, suggesting the good reversible capacity of MWNT. Fig. 5c shows the discharge–charge voltage profiles of Co_3O_4/MWNT nanocomposites electrode. In the first discharge curve, two obvious voltage plateaus at 1.2 and 1.1 V can be ascribed to the formation of CoO and amorphous Li_2O, and Co and amorphous Li_2O, respectively, which are similar to that of pure Co_3O_4 electrode. The initial discharge and charge capacities are found to be 960 and 670 mA h g^{-1}, respectively. The coulombic efficiency is 70%, much higher than that of pure Co_3O_4 and pure MWNT electrodes as aforementioned. The improvement of coulombic efficiency is attributed to the unique nanostructure of the Co_3O_4/MWNT nanocomposites. First, the entangled MWNTs connect the Co_3O_4 nanoflakes, providing the channels for the conduction of electrons and ions. Second, the intertwined MWNTs form a three dimensional network with a certain amount of flexibility, preventing the electrode from isolating or cracking.[54] The above structure improvement has facile electrochemical reaction kinetics assuring a more complete conversion reaction and higher coulombic efficiency.

Fig. 5d presents the CV curves of the Co_3O_4/MWNT nanocomposites for the first three cycles at a scan rate of 0.1 mV s^{-1}, respectively. In the first cathodic scan, a large current peak appears at 0.88 V, attributing to the reduction process of Co_3O_4 to metallic cobalt, the formation of amorphous Li_2O and the formation of SEI layers.[55] A broad anodic peak located at 2.10 V corresponds to the oxidation reaction and formation of cobalt oxide. In the second cycle, the main reduction peak is increased to 1.05 V and the peak intensity apparently decreases. Meanwhile, the oxidation peak shifts to 2.17 V and becomes wider and weaker. The third cycle displays very little modification compared with the second one, indicating superior electrochemical stability of the Co_3O_4/MWNT nanocomposites. The weak but discriminable reduction and oxidation peaks at 0.02 and 0.15 V observed in all the three cycles, respectively, are due to the insertion or extraction of Li into or from graphene layers of MWNTs, suggesting that the MWNTs in the nanocomposites are electroactive and reversible for the lithium storage.[56] In conclusion, the electrochemical reaction processes can be described as following eqn (1)–(3):[57,58]

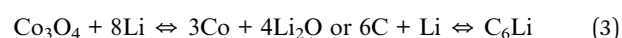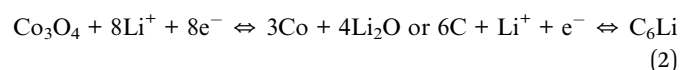$$Li \Leftrightarrow Li^+ + e^- \tag{1}$$

$$Co_3O_4 + 8Li^+ + 8e^- \Leftrightarrow 3Co + 4Li_2O \text{ or } 6C + Li^+ + e^- \Leftrightarrow C_6Li \tag{2}$$

$$Co_3O_4 + 8Li \Leftrightarrow 3Co + 4Li_2O \text{ or } 6C + Li \Leftrightarrow C_6Li \tag{3}$$

Fig. 6a and d comparatively depicts the cycling stability and rate capability of Co₃O₄/MWNT composites, pure Co₃O₄ and pure MWNT, respectively. The reversible specific capacities of the Co₃O₄/MWNT nanocomposites, pure Co₃O₄ and pure MWNTs achieve 708, 385 and 278 mA h g⁻¹ after 100 cycles at a current density of 100 mA g⁻¹, respectively (Fig. 6a). The coulombic efficiency of Co₃O₄/MWNTs reaches 98% in the initial 5 cycles, and remains more than 97% in the following cycles. For the pure Co₃O₄ electrode, the coulombic efficiency increases to 95% at the 5th cycle. It varies between 95 and 98% in the subsequent cycles. As to the pure MWNT electrode, the coulombic efficiency needs more cycles (after 18 cycles) to reach a stable value of *ca.* 96%. The gradual increase in capacity of the Co₃O₄/MWNT anode is attributed to the activation of some irreversible Li₂O generated in the first discharge step.[58–60] The Co₃O₄/MWNT nanocomposites achieve the specific capacities of 773, 805, 698, and 491 mA h g⁻¹ at the current densities of 100, 200, 400, and 800 mA g⁻¹, respectively. As the current density is returned to 100 mA g⁻¹, the specific capacity shows a great increase to 855 mA h g⁻¹. These results show that the Co₃O₄/MWNT nanocomposites electrode demonstrates a superior electrochemical performance compared to those of pure Co₃O₄ and pure MWNTs. The enhanced electrochemical performance is due to the entanglement, flexibility and conductivity of MWNTs in the nanocomposites. The FE-SEM image of the Co₃O₄/MWNT nanocomposites after cycling is shown in Fig. S2.† The Co₃O₄ nanoflakes have disappeared along with the formation of Co₃O₄ nanoparticles. The Co₃O₄ nanoparticles were partly attached on the MWNTs and dispersed well with the MWNTs. The composited structure is apparently beneficial to the conduction of electron and lithium ion. Consequently, the as-made Co₃O₄/MWNT nanocomposites exhibit enhanced cycling and rate performances.

The impedance spectra of the Co₃O₄, MWNTs and Co₃O₄/MWNTs samples were measured at charged states from different cycles in the 100 kHz to 0.01 Hz range. As reported previously, EIS contains two depressed semicircular arcs in the high and medium frequency and a straight line in the low frequency.[61,62] The impedance contains ionic resistance of the electrolyte (R_e), surface film resistance (R_{sf}) corresponding to the high frequency semicircle and charge transfer resistance (R_{ct}) attributing to the medium frequency semicircle. The impedance is in direct proportion to the diameter of the semicircle. The ($R_e + R_{sf} + R_{ct}$) values of the Co₃O₄/MWNTs electrode after 1, 3, 5, 10 and 80 cycles are 472, 1454, 1744, 1406 and 495

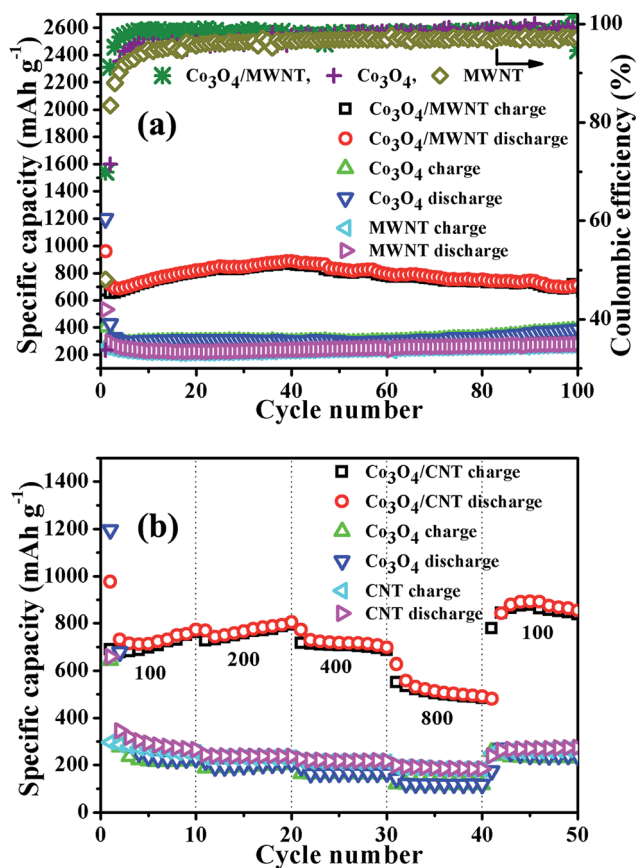Fig. 6 (a) Cycling performance and coulombic efficiency at the current density of 100 mA g⁻¹, and (b) the rate capabilities of Co₃O₄/MWNT, Co₃O₄ and MWNT.
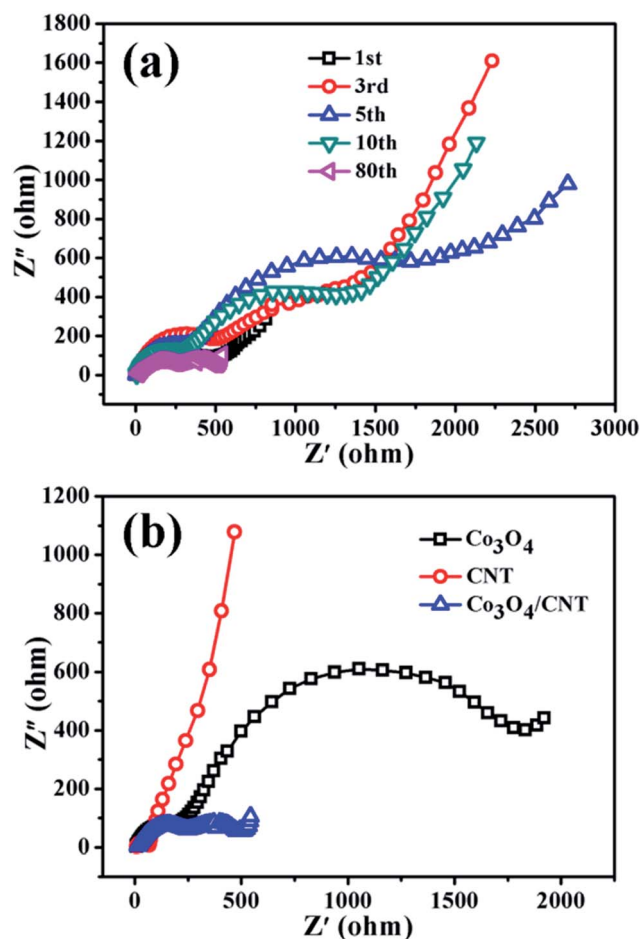

Fig. 7 (a) Nyquist plots of the sample Co₃O₄/MWNT collected from the 1st, 5th, 10th, and 80th charged states, (b) Nyquist plots of the samples Co₃O₄, MWNT and Co₃O₄/MWNT collected from the 80th charged states.

Ω, respectively (Fig. 7a). The impedance ($R_e + R_{sf} + R_{ct}$) of the Co_3O_4/MWNTs electrode tends to increase in the initial 5 cycles and then decrease in the following cycles. This phenomenon correlates well with the result that the specific capacity of the Co_3O_4/MWNT electrode reduces in the initial several cycles and then increases slowly within 40 cycles. The decrease in the impedance after the initial 5 cycles backs up the realization of the activation process. The reduction of impedance after cycling corresponds to the structure variation in the discharge–charge processes (Fig. S2†). The formation of Co_3O_4 nanoparticles composited with MWNTs results in a better conduction of electron and lithium ions. Therefore, the impedance decreases gradually after the initial 5 cycles. The ($R_e + R_{sf} + R_{ct}$) values of Co_3O_4, MWNTs and Co_3O_4/MWNTs electrodes after 80 cycles are ca. 1851, 308 and 495 Ω, respectively (Fig. 7b). Apparently, the electrical conductivity and charge transfer at the interface can be greatly improved through blending with MWNTs, which enhances the electrochemical property of Co_3O_4 as an anode material.

4. Conclusion

Well dispersed porous Co_3O_4 nanoflakes-MWNTs blended anode materials have been prepared for LIBs. The MWNTs have greatly improved the electrical conductivity and charge transfer at the interface of the as-prepared Co_3O_4/MWNT composite anode. The intertwined MWNTs with a certain amount of flexibility prevent the electrode from isolating or cracking during the lithiation/delithiation processes, resulting in a superior cycling stability and rate capability.

Acknowledgements

References

1 F. H. Du, B. Li, W. Fu, Y. J. Xiong, K. X. Wang and J. S. Chen, *Adv. Mater.*, 2014, **26**, 6145–6150.

2 X. Wang, S. Qiu, G. Lu, C. He, J. Liu, L. Luan and W. Liu, *CrystEngComm*, 2014, **16**, 1802–1809.

3 Y. P. Wu, C. Jiang, C. Wan and R. Holze, *J. Power Sources*, 2002, **111**, 329–334.

4 (*a*) D. Su, H. Ahn and G. Wang, *J. Power Sources*, 2013, **244**, 742–746; (*b*) C. Wang, Q. Li, F. Wang, G. Xia, R. Liu, D. Li, N. Li, J. Spendelow and G. Wu, *ACS Appl. Mater. Interfaces*, 2014, **6**, 1243–1250; (*c*) Z. Gao, W. Yang, J. Wang, N. Song and X. Li, *Nano Energy*, 2015, **13**, 306–317.

5 (*a*) W. Wei, Z. Wang, Z. Liu, Y. Liu, L. He, D. Chen, A. Umar, L. Guo and J. Li, *J. Power Sources*, 2013, **238**, 376–387; (*b*) C. Zhao, L. Liu, Q. Zhang, J. Rogers, H. Zhao and Y. Li, *Electrochim. Acta*, 2015, **155**, 288–296; (*c*) X. Sun, Q. Wu, X. Zhan, J. Wu, S. Wei and Z. Wei, *J. Mater. Sci.*, 2012, **47**, 2519–2534; (*d*) L. Liu, C. Zhao, H. Zhao, Q. Zhang and Y. Li, *Electrochim. Acta*, 2014, **135**, 224–231.

6 M. V. Reddy, G. V. Subba Rao and B. V. R. Chowdari, *Chem. Rev.*, 2013, **113**, 5364–5457.

7 Y. Sun, X. Feng and C. Chen, *J. Power Sources*, 2011, **196**, 784–787.

8 D. Zhang, A. Qian, J. Chen, J. Wen, L. Wang and C. Chen, *Ionics*, 2012, **18**, 591–597.

9 J. Kang, Y. Ko, J. Park and D. Kim, *Nanoscale Res. Lett.*, 2008, **3**, 390–394.

10 D. Qiu, G. Bu, B. Zhao, Z. Lin, L. Pu, L. Pan and Y. Shi, *Mater. Lett.*, 2014, **119**, 12–15.

11 (*a*) C. Hu, S. Guo, G. Lu, Y. Fu, J. Liu, H. Wei, X. Yan, Y. Wang and Z. Guo, *Electrochim. Acta*, 2014, **148**, 118–126; (*b*) J. Zhu, M. Chen, Q. He, L. Shao, S. Wei and Z. Guo, *RSC Adv.*, 2013, **3**, 22790–22824.

12 S. Guo, G. Lu, S. Qiu, J. Liu, X. Wang, C. He, H. Wei, X. Yan and Z. Guo, *Nano Energy*, 2014, **9**, 41–49.

13 H. Qu, S. Wei and Z. Guo, *J. Mater. Chem. A*, 2013, **1**, 11513–11528.

14 X. Li, H. Gu, J. Liu, H. Wei, S. Qiu, Y. Fu, H. Lv, G. Lu, Y. Wang and Z. Guo, *RSC Adv.*, 2015, **5**, 7237–7244.

15 H. Cao, X. Wang, H. Gu, J. Liu, L. Luan, W. Liu, Y. Wang and Z. Guo, *RSC Adv.*, 2015, **5**, 34566–34571.

16 C. Chae, J. H. Kim, J. M. Kim, Y. Sun and J. K. Lee, *J. Mater. Chem.*, 2012, **22**, 17870–17877.

17 J. Hwang, H. Lim, Y. Sun and K. Suh, *J. Power Sources*, 2013, **244**, 538–543.

18 I. Lahiri and W. Choi, *Crit. Rev. Solid State Mater. Sci.*, 2013, **38**, 128–166.

19 C. Xu, J. Sun and L. Gao, *J. Power Sources*, 2011, **196**, 5138–5142.

20 Z. Wang, D. Luan, S. Madhavi, Y. Hu and X. W. D. Lou, *Energy Environ. Sci.*, 2012, **5**, 5252–5256.

21 L. Noerochim, J. Wang, S. Chou, H. Li and H. Liu, *Electrochim. Acta*, 2010, **56**, 314–320.

22 M. H. Chen, Z. C. Huang, G. T. Wu, G. M. Zhu, J. K. You and Z. G. Lin, *Mater. Res. Bull.*, 2003, **38**, 831–836.

23 J. Qin, Q. Zhang, Z. Cao, X. Li, C. Hu and B. Wei, *Nano Energy*, 2013, **2**, 733–741.

24 Z. Wen, Q. Wang, Q. Zhang and J. Li, *Adv. Funct. Mater.*, 2007, **17**, 2772–2778.

25 T. H. Yoon and Y. J. Park, *Solid State Ionics*, 2012, **225**, 498–501.

26 L. Zhuo, Y. Wu, J. Ming, L. Wang, Y. Yu, X. Zhang and F. Zhao, *J. Mater. Chem. A*, 2013, **1**, 1141–1147.

27 G. Wang, X. Shen, J. Yao, D. Wexler and J. Ahn, *Electrochem. Commun.*, 2009, **11**, 546–549.

28 A. Cao, C. Xu, J. Liang, D. Wu and B. Wei, *Chem. Phys. Lett.*, 2001, **344**, 13–17.

29 H. Xia, Y. Wang, J. Lin and L. Lu, *Nanoscale Res. Lett.*, 2012, **7**(33), 1–10.

30 H. Gu, S. B. Rapole, Y. Huang, D. Cao, Z. Luo, S. Wei and Z. Guo, *J. Mater. Chem. A*, 2013, **1**, 2011–2021.

31 F. X. Wang, X. P. Gao, Z. W. Lu, S. H. Ye, J. Q. Qu, F. Wu, H. T. Yuan and D. Y. Song, *J. Alloys Compd.*, 2004, **370**, 326–330.

32 T. J. Chuang, C. R. Brundle and D. W. Rice, *Surf. Sci.*, 1976, **59**, 413–429.

33 Y. Zhang, H. Xiong, K. Liew and J. Li, *J. Mol. Catal. A: Chem.*, 2005, **237**, 172–181.

34 J. Li, Z. Jiang, K. Qian and W. Huang, *Chin. J. Chem. Phys.*, 2012, **25**, 103–109.

35 P. Konava, M. Stoyanova, A. Naydenov, St. Christoskova and D. Mehandjiev, *Appl. Catal. A: Gen.*, 2006, **298**, 109–114.

36 M. Kang, M. W. Song and C. H. Lee, *Appl. Catal. A: Gen.*, 2003, **251**, 143–156.

37 S. Kundu, Y. Wang, W. Xia and M. Muhler, *J. Phys. Chem. C*, 2008, **112**, 16869–16878.

38 R. H. Bradley, K. Cassity, R. Andrews, M. Meier, S. Osbeck, A. Andreu, C. Johnston and A. Crossley, *Appl. Surf. Sci.*, 2012, **258**, 4835–4843.

39 F. Sun, J. Gao, Y. Zhu, G. Chen, S. Wu and Y. Qin, *Adsorption*, 2013, **19**, 959–966.

40 P. Shi, X. Dai, H. Zheng, D. Li, W. Yao and C. Hu, *Chem. Eng. J.*, 2014, **240**, 264–270.

41 D. Larcher, G. Sudant, J. Leriche, Y. Chabre and J. Tarascon, *J. Electrochem. Soc.*, 2002, **149**, A234–A241.

42 C. Hu, J. Guo, J. Wen and Y. Peng, *J. Mater. Sci. Technol.*, 2013, **29**, 215–220.

43 P. Poizot, S. Laruelle, S. Grugeon, L. Dupont and J. Tarascon, *Nature*, 2000, **407**, 496–499.

44 Y. Liu, C. Mi, L. Su and X. Zhang, *Electrochim. Acta*, 2008, **53**, 2507–2513.

45 Y. J. Mai, D. Zhang, Y. Q. Qiao, C. D. Gu, X. L. Wang and J. P. Tu, *J. Power Sources*, 2012, **216**, 201–207.

46 Z. Cui, X. Guo and H. Li, *Electrochim. Acta*, 2013, **89**, 229–238.

47 Y. Kang, K. Kim, J. Kim, H. Kim, P. S. Lee, J. Lee, H. K. Liu and S. X. Dou, *J. Power Sources*, 2004, **133**, 252–259.

48 H. Liu and S. Yen, *J. Power Sources*, 2007, **166**, 478–484.

49 P. A. Connor and J. T. S. Irvine, *Electrochim. Acta*, 2002, **47**, 2885–2892.

50 Z. Fu, Y. Wang, Y. Zhang and Q. Qin, *Solid State Ionics*, 2004, **170**, 105–109.

51 G. Du, C. Zhong, P. Zhang, Z. Guo, Z. Chen and H. Liu, *Electrochim. Acta*, 2010, **55**, 2582–2586.

52 A. L. M. Reddy, M. M. Shaijumon, S. R. Gowda and P. M. Ajayan, *Nano Lett.*, 2009, **9**, 1002–1006.

53 X. X. Wang, J. N. Wang, H. Chang and Y. F. Zhang, *Adv. Funct. Mater.*, 2007, **17**, 3613–3618.

54 L. Shen, C. Yuan, H. Luo, X. Zhang, K. Xu and F. Zhang, *J. Mater. Chem.*, 2010, **21**, 761–767.

55 F. Hao, Z. Zhang and L. Yin, *ACS Appl. Mater. Interfaces*, 2013, **5**, 8337–8344.

56 Z. Wu, W. Ren, L. Wen, L. Gao, J. Zhao, Z. Chen, G. Zhou, F. Li and H. Cheng, *ACS Nano*, 2010, **4**, 3187–3194.

57 Y. Kang, M. Song, J. Kim, H. Kim, M. Park, J. Lee, H. K. Liu and S. X. Dou, *Electrochim. Acta*, 2005, **50**, 3667–3673.

58 Y. Yu, C. Chen, J. Shui and S. Xie, *Angew. Chem., Int. Ed.*, 2005, **44**, 7085–7089.

59 S. Grugeon, S. Laruelle, L. Dupont and J. M. Tarascon, *Solid State Sci.*, 2003, **5**, 895–904.

60 J. Do and C. Weng, *J. Power Sources*, 2005, **146**, 482–486.

61 G. Lu, S. Qiu, J. Liu, X. Wang, C. He and Y. Bai, *Electrochim. Acta*, 2014, **117**, 230–238.

62 J. Kang, Y. Ko, J. Park and D. Kim, *Nanoscale Res. Lett.*, 2008, **3**, 390–394.